Free Surface Flow and Heat Transfer in Conduction Mode Laser Welding

A. PAUL and T. DEBROY

Temperature profiles and fluid flow fields in a weld pool are simulated through numerical solutions of Navier-Stokes equation and the equation of conservation of energy for low power laser welding in conduction mode. Experimentally determined weld pool surface topography, peak temperature, and the secondary dendrite arm spacings are found to be in fair agreement with the corresponding theoretically calculated values.

I. INTRODUCTION

DURING laser welding of alloys, the structure and properties of the welds are influenced by the simultaneous occurrence of several important physical processes. These include the absorption of the laser beam by the weld pool surrounded by the hot plasma, heat exchange between the weld pool surface and the surroundings, vigorous circulation of molten metal resulting primarily from the spatial variation of surface tension at the weld pool surface, convective heat transfer in the molten metal, and its solidification. Much of the earlier work on these component processes was motivated by the appreciation that the improved understanding would ultimately lead to better welds. Indeed, if the weld structure and properties can be predicted from first principles of transport phenomena, it would be possible, at least in principle, to adjust welding parameters so as to achieve a desired combination of microstructure and mechanical properties.

Because of the small size of the weld pool and the presence of plasma in the vicinity of the weld pool, physical measurements of important parameters such as the temperature and velocity fields in the weld pools are not easy tasks. Therefore, much of the previous work[1-4] on the transport processes in the weld pool was based on the mathematical modeling of the essential physical features of the welding process, and the technique has been successful in revealing detailed insight about certain aspects of the welding process that cannot be obtained otherwise. However, in this approach, our inability of making important measurements is traded, to a large extent, with the difficulties involved in adequately understanding and modeling the complex component physical processes of welding. In addition, certain experimental data are required for the calculations. For example, although we can account for the attenuation of the beam energy due to the presence of the plasma by providing an experimentally determined value of absorptivity, this must be viewed as a compromise of the predictive capability of the model in our quest for accuracy. A more fundamental limitation is imposed by the lack of necessary data pertinent to the plasma-weld pool system. The primary driving force for fluid flow in the laser melted pools is the surface tension gradient. The interfacial tension between the molten metals and plasma[5] has received very little attention in the past and systematic investigations of surface tension of binary metal-solute systems[6] at temperatures much above the melting point are just beginning. Furthermore, the heat exchange between the weld pool surface and the plasma cannot be currently estimated with a reasonable degree of trustworthiness. At high laser powers, additional complexities are introduced due to the presence of the keyhole that forms during welding. In view of these uncertainties in the credible quantification of several crucial physical processes of welding, attempts to understand welding processes through simulation must include concomitant well-designed experimental work.

In this paper, the weld pool temperatures obtained from the analysis of the vapors evolved during welding are compared with the temperature values calculated from the numerical solution of the equations of change. The secondary dendrite arm spacing values, obtained from numerically computed cooling rates, are compared with the corresponding values determined from the solidification structure. The surface topography of the welds, computed as a function of time during weld pool cooling, is used to reconstruct the surface of the solidified weld by an appropriate profile superimposition technique. The computed topography is compared with the experimentally observed surface profile.

II. PROCEDURES

A carbon dioxide laser, Coherent Model Everlase 525-1, capable of producing a maximum output power of 575 watts in the continuous wave mode was used. Samples were placed on a remotely controlled, electrically operated table capable of providing linear motion. Welding was carried out inside a plexiglass box under a controlled atmosphere using a 2.54 cm diameter, 12.7 cm focal length Zn-Se lens with an antireflection coating. Most of the experiments were conducted with a high manganese stainless steel, USS Tenelon, containing 15 pct Mn, 18 pct Cr, 0.75 pct Ni, and 0.12 pct C. A few experiments were conducted with puratronic iron obtained from Johnson Mathey Chemicals Limited containing less than 10 ppm total impurities.

The effective temperature for vaporization was determined by following a technique[7] developed earlier at Penn State. The technique is based on the following principle. If the rate of loss of alloying elements is controlled by their vaporization at the weld pool surface and the rates are related to their equilibrium vapor pressures over the molten pool, the ratio of the vaporization rates of any two elements is a strong function of temperature. Alternatively, for a

A. PAUL, Graduate Student, and T. DEBROY, Associate Professor of Metallurgy, are with the Department of Materials Science and Engineering, The Pennsylvania State University, 212 Steidle Building, University Park, PA 16802.

Manuscript submitted February 17, 1988.

given composition of the molten pool, if the ratio of the vaporization rates of any two elements is known, an effective pool temperature for the vaporization of the alloying elements can be determined. During welding experiments, a portion of the vaporized material was allowed to condense in the interior surface of a hollow quartz tube. The composition of the condensate was used to determine the relative rates of vaporization of the individual elements and the effective weld pool temperature for vaporization. Details of this procedure are documented elsewhere.[7]

The equations of change for two-dimensional, transient, incompressible flow were solved numerically.[8] Since these equations are well documented in standard textbooks, these are not reproduced here. Instead, only the salient features of the computation scheme are presented here. In formulating the model, the following assumptions were made:

(1) The fluid flow and heat transfer inside the molten pool are adequately described by a two-dimensional, time-dependent, constant density representation.
(2) The flow is primarily driven by the surface tension gradient produced as a result of the temperature gradient at the surface.
(3) The welding was performed in the conduction mode (low aspect ratio welds), and key hole formation did not take place.

Calculations were performed for two mutually perpendicular planes shown in Figures 1(a) and (b). Since the transverse section of the weld pool, shown in Figure 1(a), is symmetrical about the axis of the laser beam, computations were performed in half of the plane (region ABCD). For the longitudinal plane shown in Figure 1(b), the weld pool is not symmetric about the laser beam axis and therefore calculations were performed for the entire plane (region EFGH). The enthalpy rather than temperature was considered as the dependent variable in the energy equation.

The principal boundary conditions are explained in Figure 2. At the surface of the weld pool the Marangoni effect was incorporated by equating the shear stress to the gradient of surface tension. At the solid-liquid interface, the curved weld pool boundary was approximated by a series of steps, and velocities were prescribed to be zero which amounts to an assumption of no-slip between the liquid metal and the solid surface. In the transverse cross-section of the pool, mass transfer across the center plane was zero due to symmetry. Since the heat exchange between the weld pool surface and the surroundings that contain hot plasma is not understood, the heat exchange was taken into account through an experimentally determined absorptivity value.[9,10] The heat transfer at the bottom and the sides of the plate was calculated by equating the conduction heat flux with the heat flux due to convection from the plate surface.

In the calculations of temperature and velocity fields, the pressure in the surface cells was prescribed to be equal to the atmospheric pressure (or any prescribed value). In the transverse plane, the local elevation of the surface necessary to define the surface topography, L, measured with respect to an arbitrary, fixed, horizontal plane was determined using the following equation:[11]

$$\frac{\partial L}{\partial t} + u\frac{\partial L}{\partial x} = v \qquad [1]$$

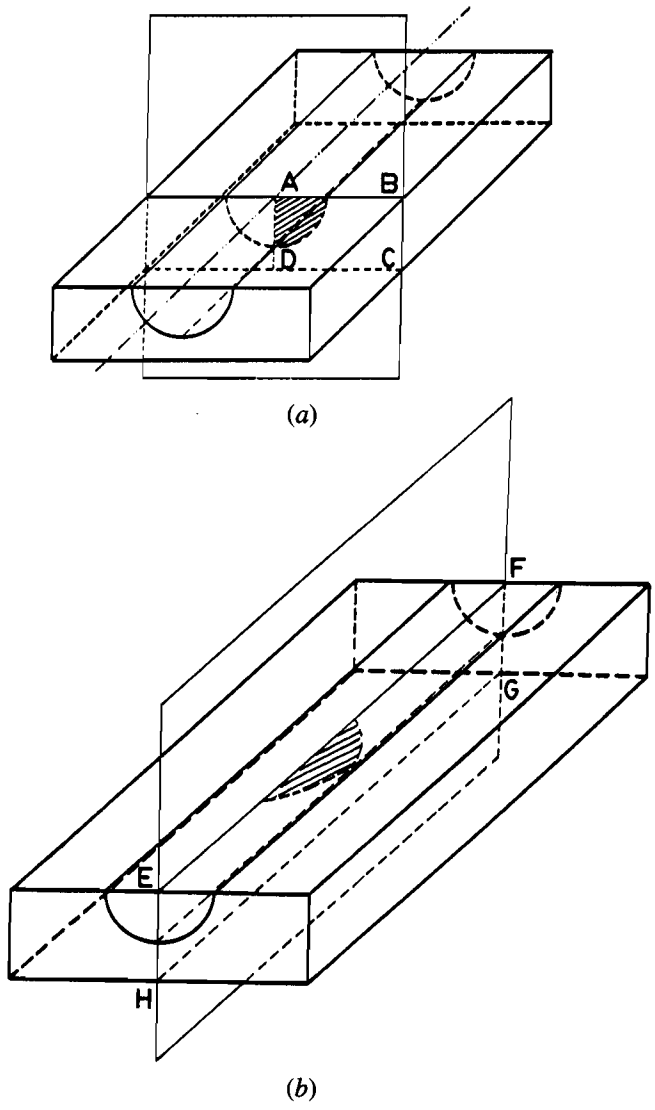

Fig. 1 — The transverse section (*a*) and the longitudinal section (*b*) of the weld as the computational domain.

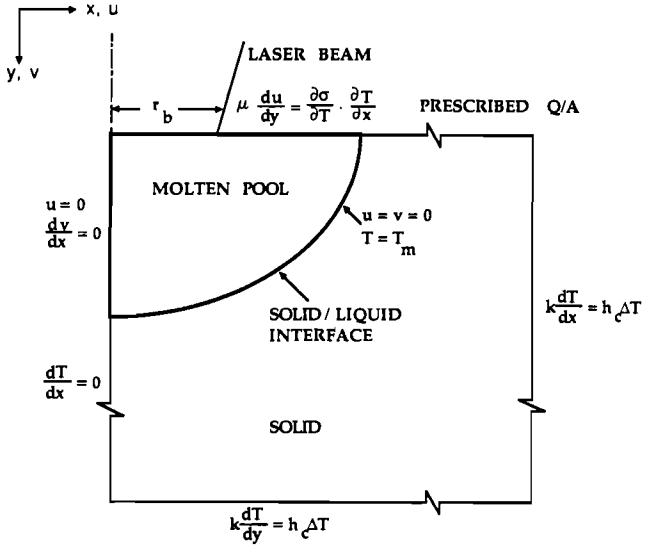

Fig. 2 — Major boundary conditions used for the solution of the equations of change.

This equation takes into account the fact that the change in surface height with time is due to the vertical (axial) velocity at the surface (v). The second term on the left-hand side is the convective term which affects the surface of the adjacent column of cells due to convection. The physical phenomena involved in the simulation of free surface flow in the longitudinal plane are somewhat more complex because of the motion of the weld pool. A discussion of coarse and fine ripple formation is presented in Reference 15, and this problem is not addressed in this paper.

An outline of the solution procedure, information on the grids used, and the stability, convergence, and accuracy of the solution are presented in the appendix.

III. RESULTS AND DISCUSSION

A. *Velocity and Temperature Profiles*

The computed temperature and velocity profiles were obtained in two mutually perpendicular planes — first, in the longitudinal section which contained the welding direction and secondly in the transverse section. The velocity profiles in the longitudinal plane at two different laser powers and welding speeds for pure iron are shown in Figure 3. The skewed nature of weld pool is clearly noted in this figure. At a constant power level, increasing the welding speed decreases the depth of penetration, which has been observed by several investigators experimentally. The velocity and temperature profiles in the transverse section for the case of pure iron are presented in Figure 4. The data used in the calculations are given in Table I. It may be noted from the velocity profile that the velocities at the surface are radially outward, resulting in a low depth-to-width ratio. The maximum velocities are of the order of 1 m/s, which is close to the figure reported by Kou and Wang[3] during the GTA welding of aluminum alloy 6061. The corresponding temperature profile indicates that the maximum weld pool temperature is 3135 K and that this temperature extends to a distance approximately equal to the radius of the laser beam. The surface temperature gradient is highest close to the laser beam and consequently the fluid velocities are also highest in the region. The existence of a strong temperature gradient in the weld pool is consistent with the absorption of a significant amount of energy in a small localized area at the center of the weld pool. The temperature distribution obtained from the solution of the equations of change needs to be validated by experimental measurements. Although the measurement of temperature distribution is not straightforward, an effective weld pool temperature may be calculated by considering the ratio of the vaporization rates of any two alloying elements. In a recent paper[12] we have demonstrated that the ratio of vaporization of alloying elements from the weld pool surface is determined by the intrinsic vaporization step. Under this condition, the ratio of the vaporization rates of any two elements i and j is given by:

$$J_i/J_j = P_i\sqrt{M_j}/P_j\sqrt{M_i} \qquad [2]$$

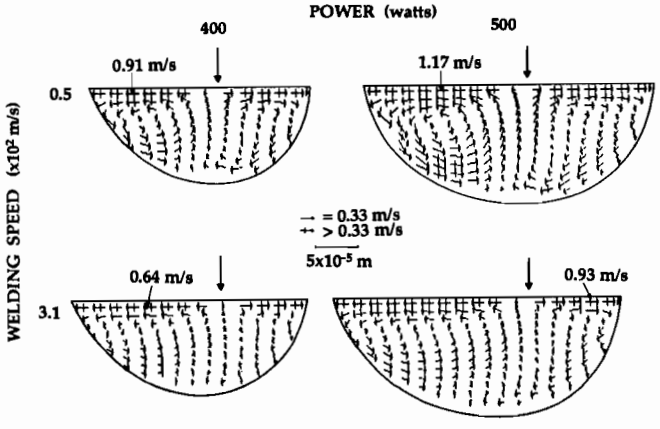

Fig. 3 — Calculated velocity profiles for pure iron in the longitudinal plane at two different powers and welding speeds.

Table I. Data Used for the Solution of the Equations of Change

Density	7.8 gm/cm^3
Thermal conductivity	0.075 cal/sec-cm-K
Specific heat	0.2 cal/gm-K
Viscosity	0.1 poise
Absorptivity	0.15
Radius of laser beam	0.0127 cm
Focal length of lens	12.7 cm
Prandtl number	1
$d\theta/dT$	−0.53 dynes/cm-K for pure Fe 0.47 dynes/cm-K for Fe + S

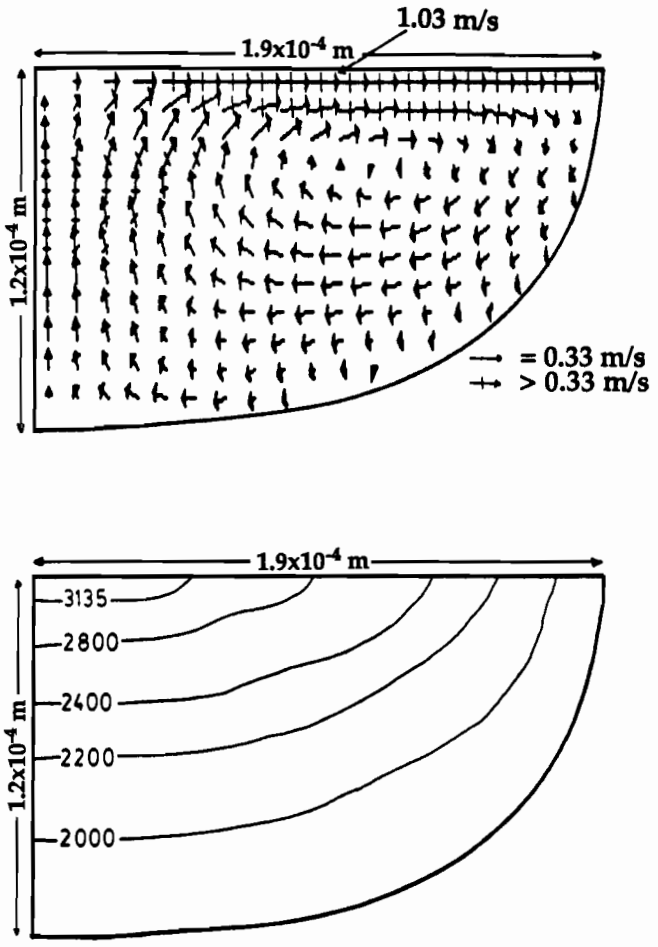

Fig. 4 — Calculated velocity and temperature profiles (in K) for pure iron in the transverse plane. Laser power 500 watts.

where J_i and J_j are the vaporization fluxes of the two elements i and j, respectively, p_i and p_j are the partial pressures, and M_i and M_j are the molecular weights.

Since P_i and P_j are strong functions of temperature, the ratio of the vaporization rates of elements i and j, (J_i/J_j), is a function of temperature. Figure 5(a) is a plot of the ratio of vaporization rates of iron and manganese *vs* temperature calculated from Eq. [2]. An experimentally obtained value of ratio of vaporization rates of iron and manganese is superimposed on this plot (shown by arrows). It is seen that the temperature corresponding to the observed ratio of the fluxes is 3070 K. A similar exercise was also conducted for the vaporization of chromium and manganese. From the results presented in Figure 5(b) a temperature of 3115 K is obtained. For both element pairs chosen, the temperature is found to be roughly equal. Since the vaporization rate is a strong function of temperature, most of the vaporized material originates from the region of highest temperature on the weld pool surface, and the effective pool temperature estimated on the basis of the vaporization of various elements is close to the maximum temperature on the weld pool surface. A comparison of the numerically predicted temperatures and those calculated from the ratio of vaporization rate of elements shows that the highest temperatures predicted by the model are very close to the effective temperatures obtained from vaporization measurements.

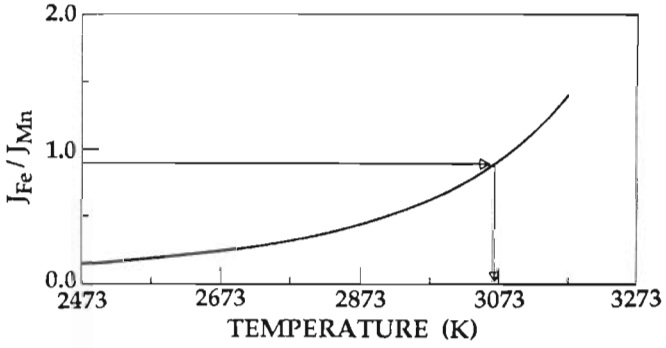

(*a*)

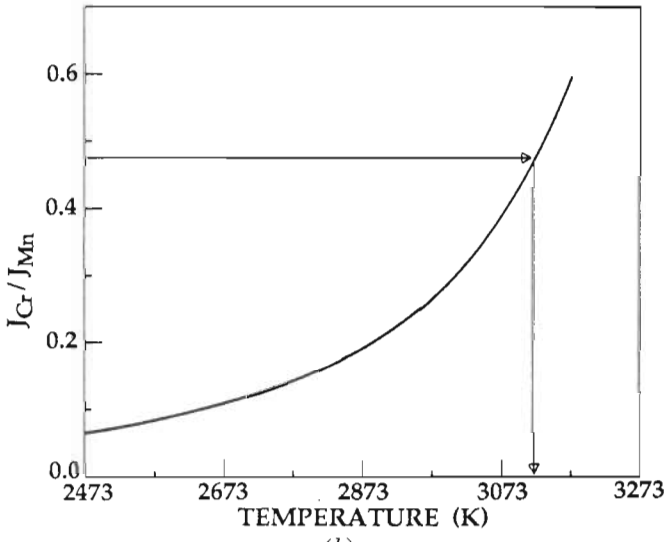

(*b*)

Fig. 5—The ratio of the calculated vaporization ratio of (*a*) iron and manganese and (*b*) chromium and manganese as a function of temperature. Horizontal solid lines represent experimentally determined vapor composition data.

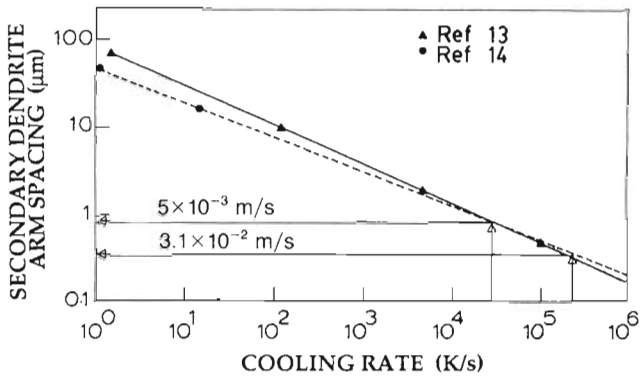

Fig. 6—Plot of secondary dendrite arm spacing as a function of cooling rate.

B. *Secondary Dendrite Arm Spacing and Cooling Rate*

Brower and Flemings[13] experimentally investigated the effect of cooling rate on the secondary dendrite arm spacing

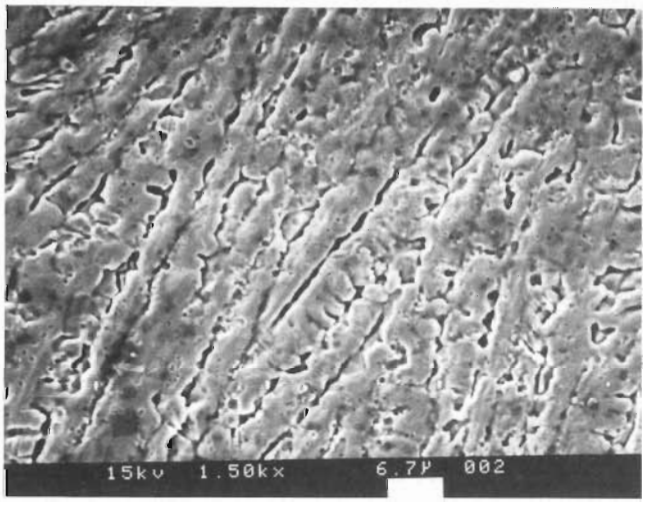

(*a*)

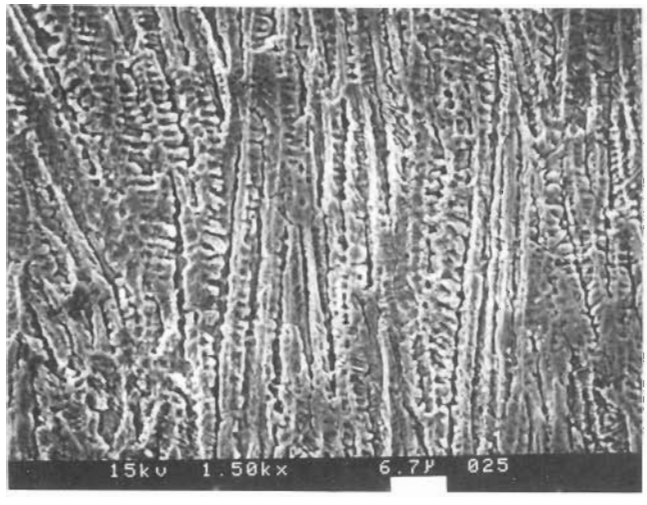

(*b*)

Fig. 7—Scanning electron micrographs of an AISI 201 sample showing secondary dendrites. Laser power: 500 watts, welding speed: (*a*) 5 mm/s and (*b*) 31 mm/s, specimen thickness: 0.7 mm.[14]

for a steel of composition similar to AISI 201 (commercial alloy 440C-17 pct Cr, 1 pct Mn). A limited number of experiments in our research group[14] at Penn State shows that the correlation between secondary dendrite arm spacing and cooling rate for AISI 201 is very close to that of the alloy 440C, as shown in Figure 6. The cooling rates at the edge of the pool were calculated from the numerically computed temperature field as the product of the temperature gradient and the welding speed, for two welding speeds, *i.e.*, 5 mm/sec and 31 mm/sec. The secondary dendrite arm spacings corresponding to these cooling rates are 2 microns and 0.4 microns, respectively. The arm spacing corresponding to a welding speed of 5 mm/sec can be readily obtained from the microstructure[14] presented in Figure 7(a). It may be seen that the arm spacing is roughly equal to that predicted by the model. The dendrite arm spacing corresponding to a welding speed of 31 mm/sec was also close to that predicted by the model. The agreement between the predicted secondary dendrite arm spacing and the values obtained from independent data demonstrates that the calculated values of cooling rates are fairly accurate.

C. *Weld Pool Surface Configurations*

The velocity and temperature fields presented so far were calculated under the assumption that the surface of the weld pool is not free to move; *i.e.*, it is a rigid surface. Although this assumption was made in all the previous works on the convection in the weld pool, in practice the surface of the weld pool moves freely. Predictions of surface configurations are important, specially for the understanding of surface topography of the welds.

Figure 8 depicts the free surface profiles of welds at different laser powers in the subkilowatt range and in the conduction mode of welding for the case of pure iron. The surface profiles shown in this figure correspond to the steady state condition. At steady state there is extensive fluid flow in the vertical direction near the center of the weld from the bottom of the pool to the top. The highest vertical velocities are in the range of 30 to 40 cm/sec. Since the surface of the weld pool is allowed to deform, the upward velocity at the center of the pool tends to elevate the surface and a hump is formed, as seen in Figure 8. Also seen in this figure is the fact that the surface is elevated at the edge of the pool in addition to the center. If the surface were assumed to be flat, there would have been a pressure build-up as a result of the fluid flow at the edge. However, since the surface is assumed to be free, and experiences a constant pressure of 1 atmosphere (Figure 9), the surface of the liquid moves up locally. From Figure 8 it is also seen that the surface unevenness decreases as the laser power is decreased. This is expected since at lower powers the fluid velocities are smaller.

In order to obtain an idea of the surface configuration after the weld pool solidified, the shape and size of the weld pool were numerically computed as a function of time after the laser was shut off. Figure 10 shows these profiles for the case of pure iron at several time instances. It is observed from this figure that as the weld pool cools, the surface unevenness becomes progressively less pronounced; nevertheless, the uneven topography is fairly visible after solidification. The reason for this may be seen in Figure 11 where the maximum radial surface velocity is plotted as a function of time after the laser beam is shut off. It is seen that as soon as the beam is shut off the velocities are high but decay rapidly as a function of time, thus decreasing the surface unevenness.

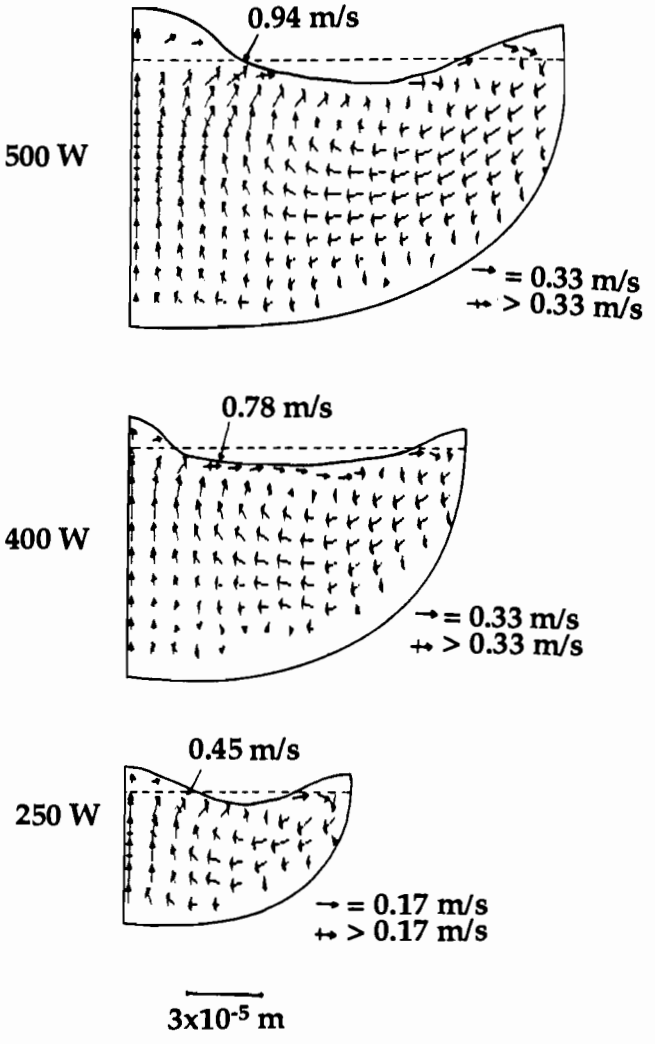

Fig. 8—Calculated surface configurations as a function of laser power.

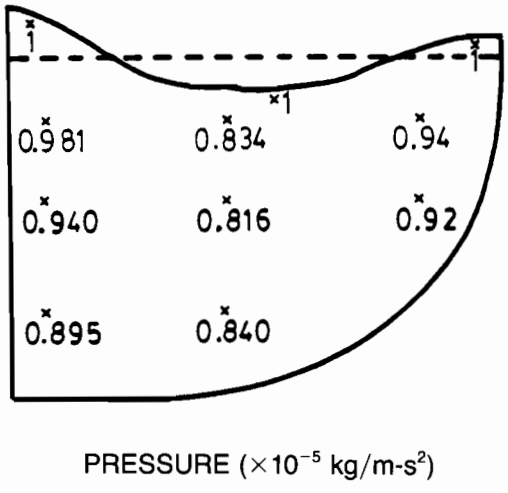

Fig. 9—Calculated pressures at several locations in the weld pool when the pool surface is considered free.

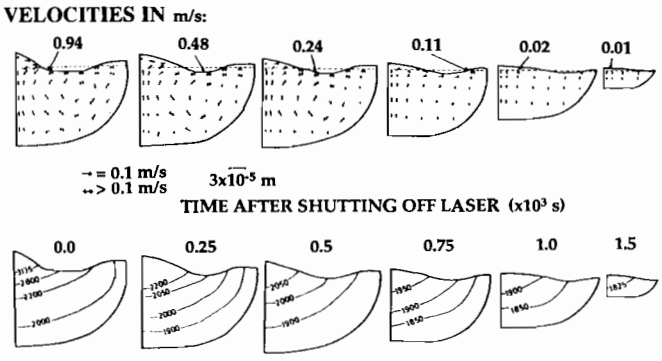

Fig. 10 — Velocity and temperature profiles (K) for pure iron as a function of time after laser was shut off.

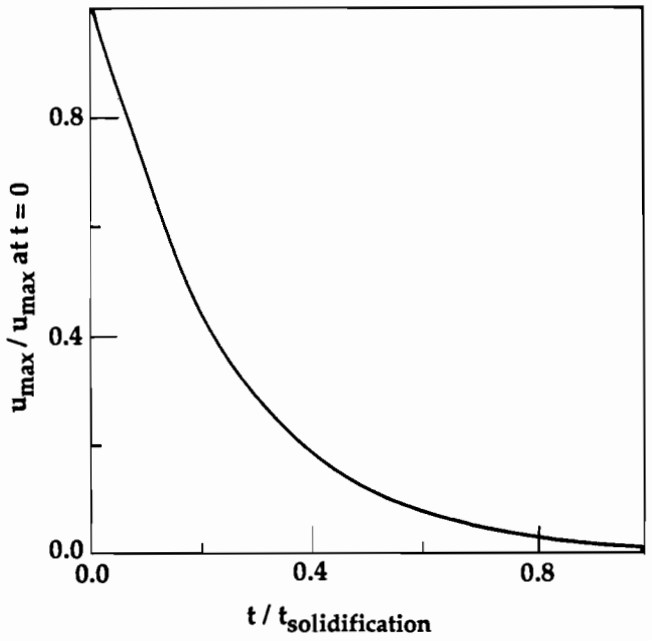

Fig. 11 — Maximum dimensionless surface velocity as a function of dimensionless time. U_{max} = 94 cm/sec, $t_{solidification}$ = 1.5 × 10^{-3} s, laser power: 500 watts.

The cooling rate was calculated as the pool cooled down when the beam was shut off. The average cooling rate of the pools shown in Figure 10 is 8.73 × 10^5 K/sec. During welding, the cooling rates are indeed expected to be lower due to the presence of the laser beam near the weld pool.

Figure 12 shows the variation of surface profiles when sulfur was present as an impurity as a function of time after the laser beam was shut off. A trend that is similar to the case for pure iron (Figure 10) is seen here. Again, the surface is elevated at the center of the pool. It is seen that the surface unevenness is higher when sulfur is present in the melt rather than when it is absent. This is expected since the fluid velocities are higher in the former case. When sulfur is present in the melt, the width of the pool decreases and therefore we have higher surface temperature gradients resulting in larger fluid velocities. The change in the density of the material was not considered for the calculations for simplicity. From Figures 10 and 12, the final pool surface profile can be obtained by superimposing the predicted surface profiles onto each other and taking the locus of the solidifying surface. The final theoretically computed surface

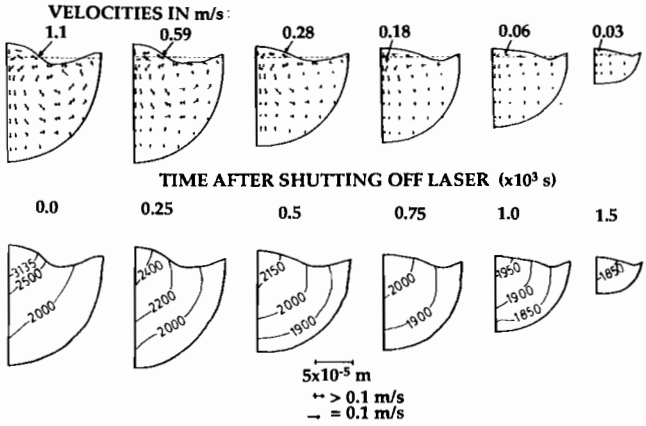

Fig. 12 — Velocity and temperature profiles for pure iron doped with sulfur as a function of time after the laser was shut off.

profiles for pure iron and iron doped with sulfur are shown in Figure 13. It is observed that the surface unevenness is more when sulfur is present in iron. This is confirmed by the experimentally observed surface profile shown in Figure 14. It is seen that the trends in the predicted surface profiles match with those observed experimentally.

IV. SUMMARY AND CONCLUSIONS

Fluid flow and heat transfer in a laser melted weld pool were investigated theoretically through incompressible, transient, two-dimensional solution of the Navier-Stokes equation and the equation of conservation of energy. Model predictions were compared with experimentally determined values of weld pool temperature, secondary dendrite arm spacings, and the weld pool surface topography. Both the computed results and the analysis of the experimental data indicated that the temperature at the laser beam–material interaction site was close to the boiling point of the alloy

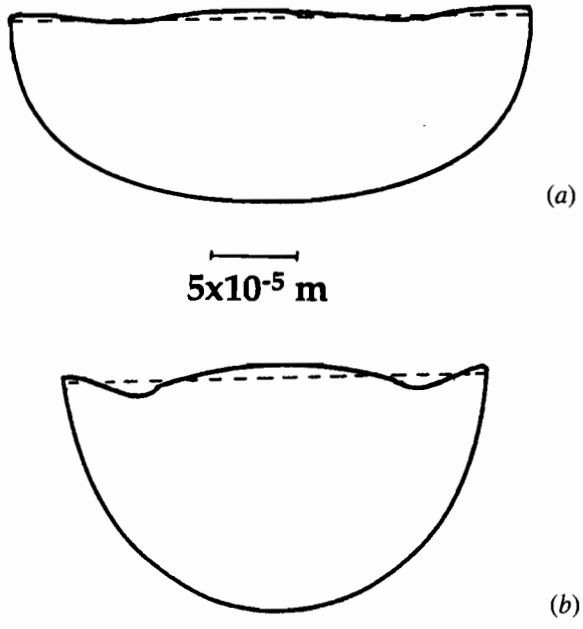

Fig. 13 — Final surface profiles predicted for the case of (*a*) pure iron and (*b*) pure iron doped with sulfur.

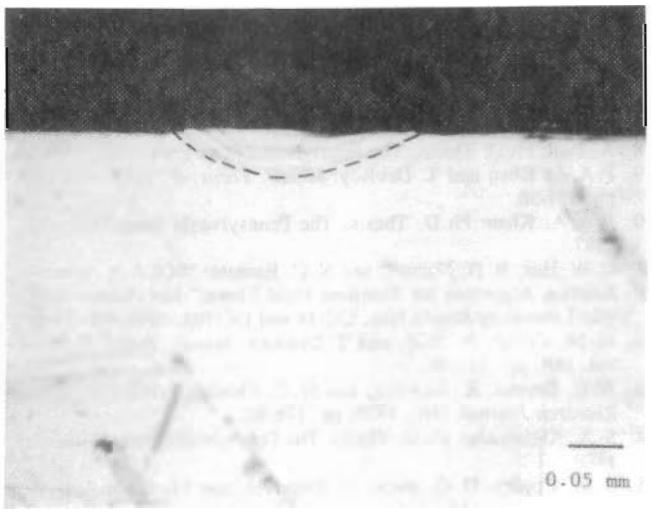

(*a*)

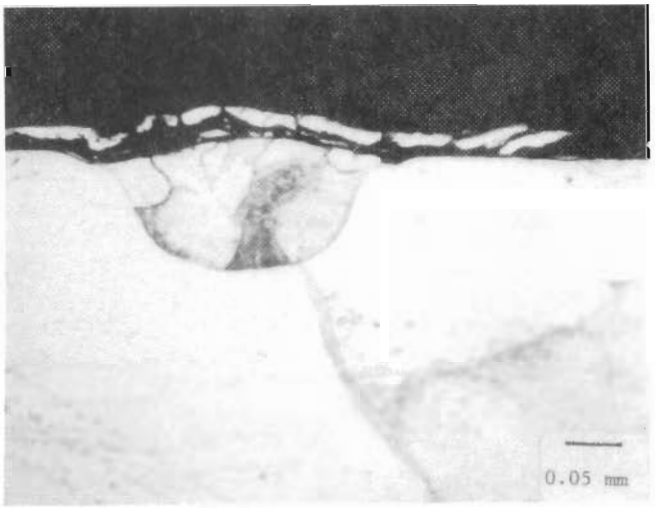

(*b*)

Fig. 14 — Optical micrographs of weld cross-section in the transverse direction for (*a*) pure iron and (*b*) iron doped with sulfur. Laser power: 500 watts, welding speed: 5 mm/sec, gas flow: 6 l/min of helium, and sample thickness: 2 mm.

for subkilowatt conduction mode laser welding. The weld pool was found to be well mixed with maximum velocities of the order of about 1 m/s, which is in agreement with the previous independent investigations. It was demonstrated that the secondary dendrite arm spacings corresponding to the predicted cooling rates were in fair agreement with those determined from independent experiments. The surface topography of the weld pool was significantly uneven. The extent of surface deformation was pronounced during welding but became less pronounced during solidification of the weld pool. The computed surface topography agreed to a fair extent with those observed experimentally. The surface unevenness was more when sulfur was present in the weld pool.

APPENDIX

Outline of the solution procedure

The equations of change were approximated by a finite difference representation and solved on a line-by-line basis using an implicit technique utilizing the tri-diagonal matrix algorithm (TDMA). The solution procedure for the equations of change in the transverse plane is outlined below.

(1) The solution is started wth known values of enthalpy at all locations in the sample. The velocities and the pressure fields are also known (usually zero) at the beginning.
(2) The energy equation is solved for the entire computational domain using the TDMA.
(3) The pool shape and size are determined depending upon the local values of the enthalpies.
(4) The momentum equations are solved in the molten pool on a line-by-line basis using TDMA.
(5) The mass imbalances in each cell are computed and the pressure and the velocities are updated accordingly (*i.e.*, to make the divergence in each cell equal to zero). If there is net outflow of mass from a cell, then the pressure is reduced and *vice versa*. Steps (2) through (5) are repeated to seek convergence.
(6) The values of enthalpy and velocities are saved and computations are completed up to a predetermined time.
(7) Steps 1 through 6 were repeated until steady state was reached or computations were completed up to a predetermined time.

In the longitudinal plane, the laser beam scanned the surface of the sample. The position of the beam varied depending upon the speed of welding. Therefore, the source term was calculated after each cycle.

When the surface was considered free, the calculations were started with approximate velocity, pressure, and temperature distributions obtained from initial calculations for a rigid surface. The pressure field was then modified by a constant factor so that the average pressure at all surface cells was equal to the applied pressure. When the momentum equations were solved, the v-velocity (velocity normal to the surface) was calculated so as to make mass divergence in the cells equal to zero. The height of the free surface was calculated by solving the kinematic equation. The procedure was repeated to achieve convergence.

Nonuniform, fixed, rectangular grids were used. Finer grids were utilized near the center region, where the laser beam impinges the surface of the material, and relatively coarse grids were used far from the axis of the laser beam. Typically a 40 × 30 grid was used with at least 5 grid points under the laser beam. A parametric study indicated that time increments less than 0.001 second did not give any different results for a minimum grid spacing of 0.001 cm in the x and y directions. Therefore, in the subsequent calculations, the time increment was taken as 0.001 seconds.

The maximum permissible mass imbalance in each cell was less than 1 pct of a reference mass divergence. The value of this reference divergence was taken as 5000 s^{-1} for a minimum grid spacing of 0.001 cm. The momentum and enthalpy convergence was achieved when u, v, and H satisfied the momentum, continuity, and enthalpy equations simultaneously.

Unconditional stability was achieved because the solution procedure was an implicit one. Thus, an unduly small time increment mandated by an explicit scheme was not required. This was a major advantage since the weld pools were very small for low power laser welding, requiring very small space and time increments to achieve stability and adequate accuracy of solution.

REFERENCES

1. G. M. Oreper and J. Szekely: *J. Fluid Mech.*, 1984, vol. 147, pp. 53-79.
2. C. Chan, J. Mazumder, and M. M. Chen: *Metall. Trans. A*, 1984, vol. 15A, pp. 2175-84.
3. S. Kou and Y. H. Wang: *Welding J. Res. Suppl.*, March 1986, pp. 63s-70s.
4. T. Zacharia, A. H. Eraslan, and D. K. Aidun: *Weldng J. Res. Suppl.*, 1988, pp. 18s-27s.
5. P. Sahoo and T. DebRoy: *Metall. Trans. B*, 1987, vol. 18B, pp. 597-601.
6. P. Sahoo, T. DebRoy, and M. J. McNallan: *Metall. Trans. B*, 1988, vol. 19B, pp. 483-91.
7. P. A. A. Khan and T. DebRoy: *Metall. Trans. B*, 1984, vol. 15B, pp. 641-44.
8. A. Paul: Ph.D. Thesis, The Pennsylvania State University, 1987.
9. P. A. A. Khan and T. DebRoy: *Metall. Trans. B*, 1985, vol. 16B, pp. 853-56.
10. P. A. A. Khan: Ph.D. Thesis, The Pennsylvania State University, 1987.
11. C. W. Hirt, B. D. Nichols, and N. C. Romero: "SOLA-A Numerical Solution Algorithm for Transient Fluid Flows," Los Alamos Scientific Laboratory Report Nos. UC-34 and UC-79d, 1975, pp. 24-26.
12. M. M. Collur, A. Paul, and T. DebRoy: *Metall. Trans. B*, 1987, vol. 18B, pp. 733-40.
13. W. E. Brower, R. Strachan, and M. C. Flemings: *AFS Cast Metals Research Journal*, Dec. 1970, pp. 176-80.
14. S. A. Abdulgadar: Ph.D. Thesis, The Pennsylvania State University, 1988.
15. S. M. Copley, D. G. Beck, D. Esquivel, and M. Bass: *Lasers in Metallurgy*, K. Mukherjee and J. Mazumder, eds., TMS-AIME, 1981, pp. 11-19.